RESEARCH ARTICLE

ADVANCED MATERIALS INTERFACES Open Access

www.advmatinterfaces.de

Check for updates

Strong Substrate Influence on Atomic Structure and Properties of Epitaxial VO_2 Thin Films

Atul Atul, Majid Ahmadi, Panagiotis Koutsogiannis, Heng Zhang, and Bart J. Kooi**

The metal–insulator transition (MIT) observed in vanadium dioxide has been a topic of great research interest for past decades, with the underlying physics yet not fully understood due to the complex electron interactions and structures involved. The ability to understand and tune the MIT behavior is of vital importance from the perspective of both underlying fundamental science as well as potential applications. In this work, scanning transmission electron microscopy (STEM) is used to investigate cross-section lamella of the VO_2 films deposited using pulsed laser deposition on three substrates: c-cut sapphire, TiO_2(101) and TiO_2(001). Advanced STEM imaging is performed in which also the oxygen atom columns are resolved. The overall film quality and structures on atomic and nanoscale are linked to the electrical transition characteristics. Relatively poor MIT characteristics are observed on c-sapphire due to the presence of very small domains with six orientation variants, and on TiO_2 (001) due to the presence of cracks induced by stress relaxation. However, the MIT on TiO_2 (101) behaves favorably, despite similar stress relaxation which, however, only leads to domain boundaries but no cracks.

1. Introduction

Metal–insulator transitions (MITs) have been extensively studied for decades owing to their importance in fundamentals of condensed matter physics[1,2] as well as for their (opto)electronic applications.[3–6] The most famous transition metal oxide showing MIT is vanadium dioxide (VO_2), which exhibits a first-order transition in bulk form just above room temperature, at 340 K,[7,8] from a low-temperature insulating phase to a high-temperature conducting phase. This is accompanied with a structural phase transition from monoclinic (M_1) crystal with space group 14 (P-21/c) to a tetragonal (rutile-R) crystal with space group 136 (P-42/mnm).[9,10] Due to the complex nature of the correlated electron interactions including a variety of intermediate states,[11–14] the transition is still not fully understood.[15–18] VO_2 is considered as a promising candidate for oxide-based electronic applications[19,20] due to its excellent transition characteristics of ultrafast resistivity change of over four orders of magnitude with a sharp hysteresis.[1,21] This MIT behavior can be further tuned by external stimuli like electric and magnetic field, light, doping, and strain.[22–27]

VO_2 thin films have been previously grown using diverse techniques, both physical and chemical, on a variety of substrates.[28–32] For such epitaxially grown films, the nature of the microstructure, including distribution of differently oriented grains and their grain boundaries, strongly affect the transition properties.[33–35] Such studies have been performed individually on the most common substrates used for growing VO_2 – sapphire[36–42] and TiO_2,[43–47] but we could not find any studies of such films and their microstructure across substrates using very similar growth conditions to maximize their comparison. Furthermore, the microstructure has been commonly studied using diffraction and in fewer cases with direct imaging using scanning transmission electron microscopy (STEM). However, then only the high-angle annular dark field (HAADF) mode was used that does not allow imaging of the O atomic columns next to the heavier V atomic columns. Another challenge is that the microstructure is not fully resolved using only plan-view studies, and cross-section preparation (e.g., by focused ion beam (FIB)) often lead to surface amorphization and damage making proper analysis difficult, especially when combined with the presence of features like domain boundaries and cracks in the films.[46]

Here we study the transition properties of VO_2 films grown on different substrates using pulsed laser deposition (PLD) under similar growth conditions, except for different growth temperatures needed to obtain epitaxial films with little inter-diffusion of layers. We correlate the differences in the MIT behaviour, as seen from Van der Pauw electrical measurements, to the structures obtained from X-ray diffraction (XRD), which show the significantly different strain profiles of the films. To understand the origin of these differences at the nanoscale, we make cross-section

A. Atul, M. Ahmadi, P. Koutsogiannis, H. Zhang, B. J. Kooi
Zernike Institute for Advanced Materials
University of Groningen
Nijenborgh 4, Groningen 9747 AG, The Netherlands
E-mail: a.atul@rug.nl; b.j.kooi@rug.nl

P. Koutsogiannis
Instituto de Nanociencia y Materiales de Aragón
Universidad de Zaragoza-CSIC
Zaragoza 50018, Spain

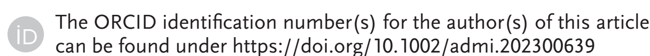
The ORCID identification number(s) for the author(s) of this article can be found under https://doi.org/10.1002/admi.202300639

© 2023 The Authors. Advanced Materials Interfaces published by Wiley-VCH GmbH. This is an open access article under the terms of the Creative Commons Attribution License, which permits use, distribution and reproduction in any medium, provided the original work is properly cited.

DOI: 10.1002/admi.202300639

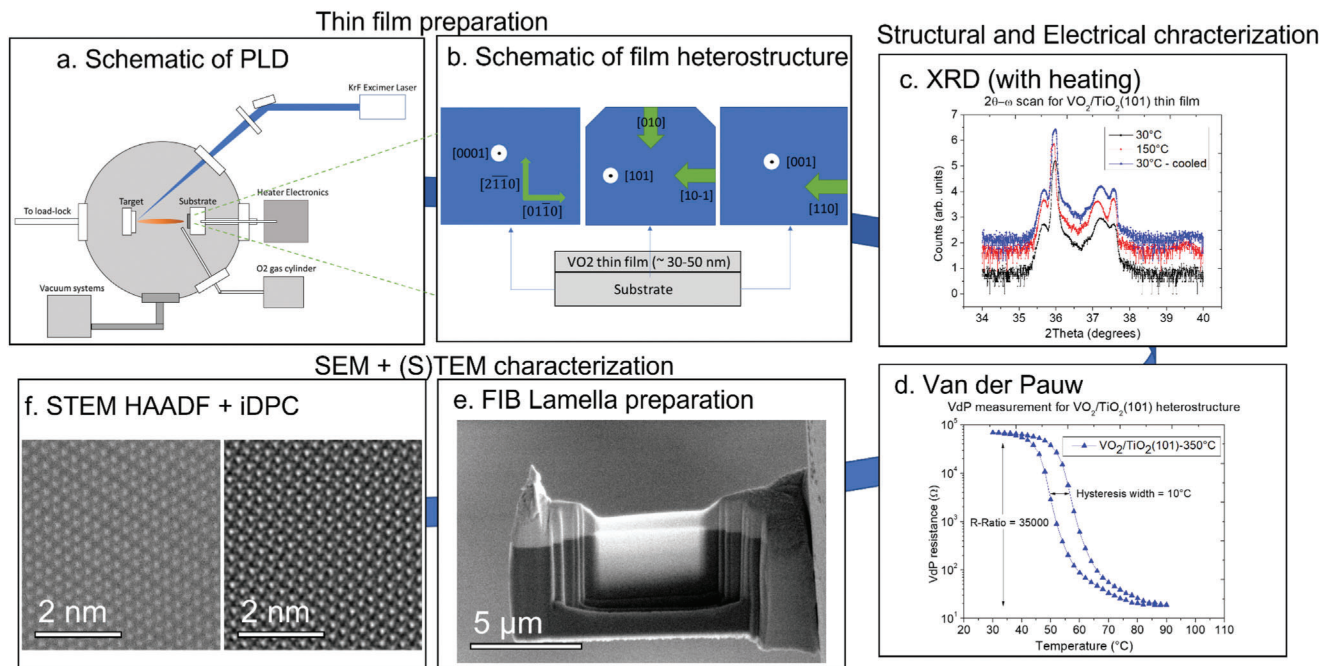

Figure 1. Schematic representation of the experiments involved in the present work. Using a) pulsed laser deposition (PLD), and b) epitaxial VO_2 films are grown on c-sapphire, TiO_2(101) and TiO_2(001) substrates. They are characterized using c) X-ray diffraction for structure, and d) Van der Pauw for sheet resistivity measurements across the transition. e) Cross-section lamella from the three films are made using a focused ion beam system, and these lamella are analyzed using f) advanced scanning transmission electron microscopy (STEM).

lamella along non-equivalent orientations from the films which are thinned at temperatures well below 0°C to prevent damage and amorphization, and then study them using STEM, combining the common HAADF imaging mode with integrated differential phase contrast (iDPC)-STEM imaging[48] where the oxygen atomic columns are also well resolved. The basic scheme of experiments involved in the present work is illustrated in **Figure 1**. The combination of the experiments described here give an unprecedented detailed and comprehensive picture of the morphology of the films on various substrates and its relation to the MI transition properties, which is of vital importance when making devices based on these films.

2. Results and Discussion

2.1. Structural and Electrical Characterization

In **Figure 2**a–c, we show scanning electron microscopy (SEM) images of the surfaces of VO_2 thin films deposited on c-cut sapphire, TiO_2(101) and TiO_2(001) substrates (taken with Ion Conversion and Electron detector), with the schematic orientations of the substrates given in the insets. From the SEM images, we can see that VO_2 on sapphire has very small grains (<100 nm), whereas the VO_2 films on both TiO_2 substrates do have domains on μm length scale. On TiO_2(101), the domain boundaries are all perpendicular to the (010) edge plane. This leads to high aspect ratio domains with widths <1 μm, but being very long parallel to the boundaries. On TiO_2(001), the domain boundaries are perpendicular to both {110} edge planes which give individual grains of variable lengths and widths, but one of these dimensions is usually of the order of ≈0.5–1 μm.

The X-ray diffraction (XRD) 2θ-ω scans of the films with 2θ values in the range 20–100° and intensity in log scale are shown in Figure 2d with vertical offsets between the scans for clarity. VO_2 on sapphire has a broad peak near 40.1° close to the very sharp (0006) peak of the substrate at 41.68°, and similarly a broad peak at 86.4° close to (00 12) peak of c-Al_2O_3 at 90.818°. The peak has previously been reported as being either (020) or (002) of monoclinic (M1) VO_2,[49–51] as both of them give very similar 2θ values, which implies that the film as-cooled down after high temperature growth has either b- or c- axis out-of-plane, respectively. It is not possible to differentiate between those peaks with 2θ-ω scans or even reciprocal space maps.[51] On TiO_2(101), there is a sharp M1 VO_2(101) peak at 37.31° close to the (101) substrate peak at 36.08°, and M1 VO_2(202) peak close to (202) substrate peak at 76.53°.[52] The reciprocal space map around the (101) peak in Figure 2g shows us the in-plane epitaxial relationship with strain around both the film and substrate peaks. On TiO_2(001), a sharp substrate peak (002) at 62.8° can be seen, with a major film peak at 65.3° with a shoulder peak at 65.8°. The reciprocal space mapping around the (002) peak also shows the in-plane orientation matching, but with a significant strain (gradient) component of the film peak which is an indication of an interface layer.[53,54] Overall, the XRD results clearly demonstrate the highly epitaxial nature of the films.

The results of Van der Pauw (VdP) electrical measurements in Figure 2e highlight the effects of these structural differences and in particular, the effect of the domain boundaries on the electrical properties. The VdP results for all the samples on the three

© 2023 The Authors. Advanced Materials Interfaces published by Wiley-VCH GmbH

21967350, 2024, 3, Downloaded from https://onlinelibrary.wiley.com/doi/10.1002/admi.202300639 by Universidad De Zaragoza, Wiley Online Library on [12/02/2024]. See the Terms and Conditions (https://onlinelibrary.wiley.com/terms-and-conditions) on Wiley Online Library for rules of use; OA articles are governed by the applicable Creative Commons License

21967350, 2024, 3, Downloaded from https://onlinelibrary.wiley.com/doi/10.1002/admi.202300639 by Universidad De Zaragoza, Wiley Online Library on [12/02/2024]. See the Terms and Conditions (https://onlinelibrary.wiley.com/terms-and-conditions) on Wiley Online Library for rules of use; OA articles are governed by the applicable Creative Commons License

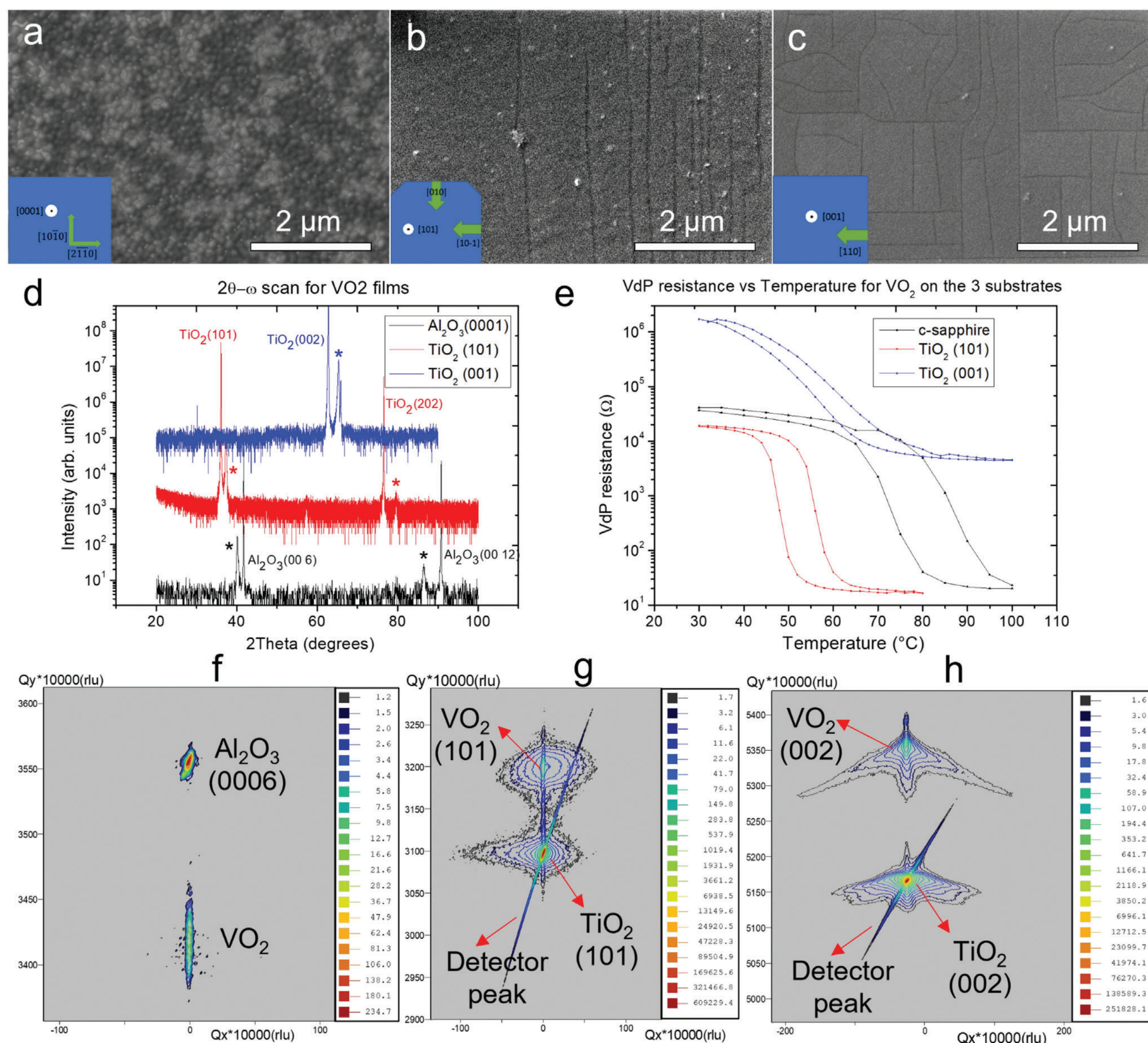

Figure 2. SEM image of the VO_2 surface on a) c-cut sapphire, b) TiO_2(101), and c) TiO_2(001) with orientation of the substrates indicated by the insets, d) XRD 2θ-ω scans of the films with vertical offsets (with peaks from VO_2 films marked with *), and e) Sheet resistance of the films as a function of temperature measured using Van der Pauw technique. Reciprocal space maps of f) VO_2 on c-sapphire around (0006) peak of Al_2O_3, g) VO_2 on TiO_2(101) around (101) peak of TiO_2, and h) VO_2 on TiO_2(001) around (002) peak of TiO_2.

substrates are provided in Figure S2 (Supporting Information), with all the transition parameters in Table S2 (Supporting Information). The samples chosen for comparison in Figure 2e are all made using 20 000 pulses under oxygen pressure of 7.5 mtorr, with the sapphire substrate kept at 500 °C and the TiO_2 substrates at 375°C, but similar trends are seen with other samples. The films on all the substrates exhibit an insulator-to-metal (or semiconductor) transition upon heating and return to the original state upon cooling. Note that we also did grow amorphous VO_2 films at room temperature on c-sapphire, followed by annealing at high temperature (500 °C). These films also show a transition (observed both electrically using Van der Pauw measurement, and optically using ellipsometry), but the change in resistance is only about one order in magnitude, and the hysteresis is much wider. This means that the starting structure of the films has large effect on the transition between rutile and monoclinic VO_2. Therefore, all films discussed in the remainder of this paper were deposited at high temperature to get better MIT characteristics. However, when electrical properties of films on various substrates are compared, the sheet resistance of the high-temperature state is of the order of 101 Ohms for films on c-sapphire and TiO_2(101), whereas it is ≈103 Ohms or higher for films on TiO_2(001) which suggests that the low-resistance state on TiO_2(001) is still a semi-conducting state instead of being the expected metallic one. Furthermore, there are also notable differences in the shape of the hysteresis curves of the

 © 2023 The Authors. Advanced Materials Interfaces published by Wiley-VCH GmbH

21967350, 2024, 3, Downloaded from https://onlinelibrary.wiley.com/doi/10.1002/admi.202300639 by Universidad De Zaragoza, Wiley Online Library on [12/02/2024]. See the Terms and Conditions (https://onlinelibrary.wiley.com/terms-and-conditions) on Wiley Online Library for rules of use; OA articles are governed by the applicable Creative Commons License

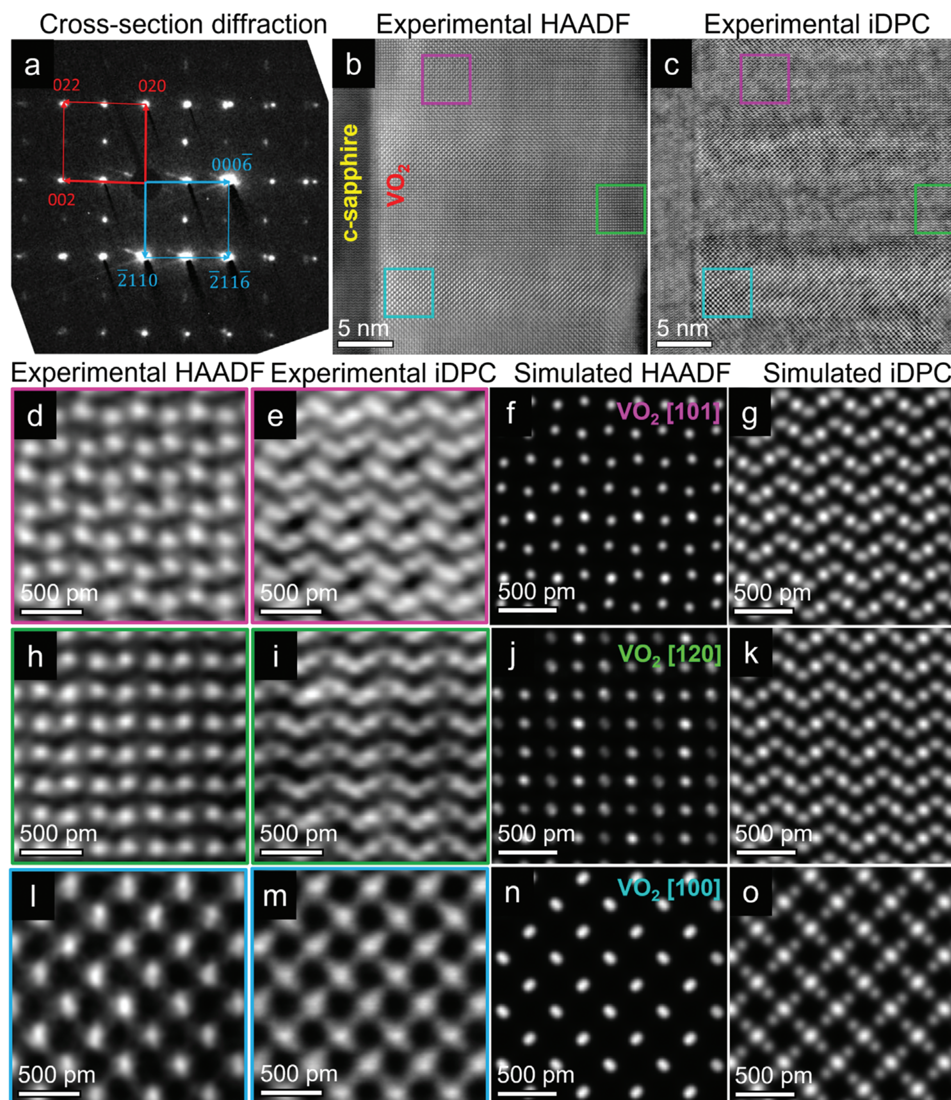

Figure 3. (S)TEM HAADF and iDPC images taken at 300 kV, and simulations for M1 VO_2 on c-cut sapphire. a) Diffraction pattern of the lamella prepared parallel to the long side of the substrate, b,c) HAADF, iDPC image for lamella with $[01\bar{1}0]$ projection axis of c-cut sapphire, with VO_2 domains of different orientations identified by comparing to corresponding simulations. Individual grains are cropped for clarity. The HAADF and iDPC of different grains with their simulations are d–g) along [101], h–k) along [120], and l–o) along [100] of VO_2.

samples on the different substrates. The samples on TiO_2(101) exhibit high quality transition characteristics, with a high resistance ratio of ≈103 with a hysteresis width of less than 10 °C. The transitions on sapphire and TiO_2(001) show similar resistance ratios, but occur over a much wider temperature range, >30 °C, even if the hysteresis width, measured as the difference in temperatures where the derivatives of resistance versus temperature show extrema, is of the same order for all three substrates. A plausible explanation could be the differences in the domain structures. For instance, the domains on TiO_2(001) could individually have a sharp transition, but the presence of multiple differently oriented domains smear out the transition over a wide temperature range. Domains, all being oriented along the same direction on TiO_2(101) substrate then leads to a significantly sharper transition. However, this reasoning clearly does not extend to c-sapphire which has a finer domain structure than TiO_2 visible in SEM images, but still has a wider transition than TiO_2(101). To further elucidate the reasons for these differences (in Figure 2e), we performed a comprehensive STEM analysis from cross-section lamellas prepared from these films, which will be discussed below.

2.2. VO_2 on Sapphire

Cross-section lamellas were prepared parallel to the short and long sides of the substrate with the directions schematically shown in Figure 2a. In **Figures 3**a and 4a, we show the selected area electron diffraction patterns obtained from the two lamella with the reciprocal lattice vectors of the substrate and film in blue and red color, respectively. The diffraction spots were indexed using the c-sut sapphire as calibration reference,

© 2023 The Authors. Advanced Materials Interfaces published by Wiley-VCH GmbH

ADVANCED MATERIALS INTERFACES
Open Access
www.advmatinterfaces.de

21967350, 2024, 3, Downloaded from https://onlinelibrary.wiley.com/doi/10.1002/admi.202300639 by Universidad De Zaragoza, Wiley Online Library on [12/02/2024]. See the Terms and Conditions (https://onlinelibrary.wiley.com/terms-and-conditions) on Wiley Online Library for rules of use; OA articles are governed by the applicable Creative Commons License

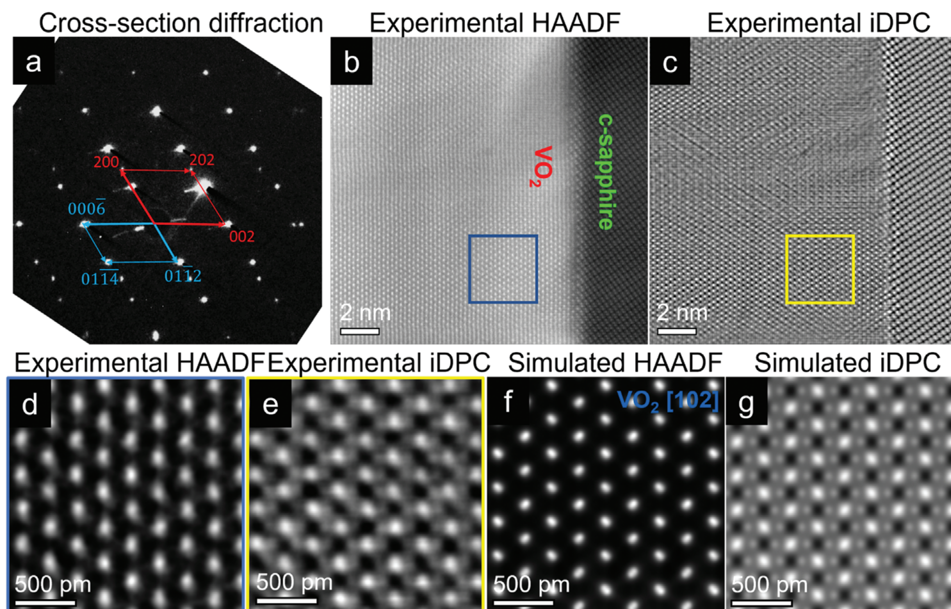

Figure 4. (S)TEM HAADF and iDPC images taken at 300 kV, and simulations for monoclinic VO_2 on c-cut sapphire. a) Diffraction pattern of the lamella prepared parallel to the short side of the substrate, b,c) HAADF, iDPC image for lamella with $[2\bar{1}\bar{1}0]$ projection axis of c-cut sapphire. HAADF and iDPC of M1 VO_2 [102] domain has been cropped in (d,e), identified by comparing to the simulations shown in (f,g).

specifically using the (0006) peak of Al_2O_3. In Figure 3a the (0006) spot of Al_2O_3 is parallel to the VO_2 spot at 0.441 $Å^{-1}$, which is the (002) peak of monclinic (M1) VO_2 as discussed before. This gives us $(000\bar{6})_{Al2O3}||(002)_{VO2}$, and the presence of the $(\bar{2}110)$ and $(\bar{2}11\bar{6})$ diffraction spots gives us the zone-axis $[01\bar{1}0]$. Overall, we get $[01\bar{1}0]_{Al2O3}||[100]_{VO2}$ and $(000\bar{6})_{Al2O3}$ || $(002)_{VO2}$ as the orientation relationship between the film and substrate. However, note that the d-spacings of (020) and (002) are very similar, so that the orientation could also be written as $[01\bar{1}0]_{Al2O3}$ $||[100]_{VO2}$, and $(000\bar{6})_{Al2O3}$ || $(020)_{VO2}$. Similarly, the $(000\bar{6})$ and $(01\bar{1}2)$ spots in Figure 4a give us, as expected, the orthogonal zone-axis $[2\bar{1}\bar{1}0]$ for the 2nd lamella,which is in agreement with previous work.[51] Overall, we get $[2\bar{1}\bar{1}0]_{Al2O3}$ || $[010]_{VO2}$, and $(000\bar{6})_{Al2O3}$ || $(002)_{VO2}$ as the orientation relationship between the film and substrate. Since the c-axis of sapphire (space group R-3c) is a threefold axis, this means that the film is composed of three distinct domains with mutual in-plane rotation[55,56] around the two growth axes (which are all shown in Figure S6, Supporting Information) giving a pseudo sixfold symmetry in the diffraction pattern. Further investigations were done based on atomic resolution STEM analysis using both High-Angle Annular Dark Field (HAADF) and Integrated Differential Phase Contrast (iDPC) images and also closely comparing experimental and simulated images.

Overview STEM HAADF and iDPC images of the two lamellas with orthogonal orientations are shown in Figures 3b,c and 4b,c, respectively. From these images, domains with different orientations can be readily identified, and from individual domains images are cropped and shown in Figures 3d–o and 4d–g. The domains have a columnar shape with a diameter not exceeding 10 nm and have a nearly uniform width over the entire film thickness. From lamella prepared along the $[01\bar{1}0]_{Al2O3}$ projection axis, three distinct domains in M1 VO_2 have been identified.

The simplest domain of these three is shown in Figure 3l,m, with V–V distances of 0.336 nm. This is easily identified as the [100] zone axis from the symmetry of the V–V distances which are 0.328 nm in the corresponding simulations in Figure 3n,o. The difference with the distances seen experimentally could be due to the domain being very close to the interface where it has high strain due to the lattice mismatch. This domain orientation is possible with either b or c out-of-plane growth axis, as seen from Figure S5 (Supporting Information).

Figure 3d,e show images of a domain with alternating short and long bonds parallel to the interface with V—V bond distances of 0.298 and 0.218 nm for long and short bonds respectively. Perpendicular to the interface there is a zig-zag pattern observable in the iDPC image, i.e., when including the oxygen atomic columns. This matches well to the model of [101] zone axis, and the corresponding simulations in Figure 3f,g clearly show the long and short bonds being 0.296 and 0.223 nm parallel to the interface and the zigzag pattern in the iDPC image perpendicular to the interface. So, this domain has grown with the b-axis out-of-plane.

Another zone axis, shown in Figure 3h,i, does not produce a structure having long and short alternating V—V bonds in either of the directions parallel and perpendicular to the interface (see Figure 3h). Still, there is a clear zig-zag pattern perpendicular to the interface present in the iDPC image (Figure 3i). The observed structure is very close to the model of the [120] zone-axis. Simulated HAADF and iDPC images for this zone-axis, shown in Figure 3j,k, respectively, agree well with the experimental images. So this domain has the degenerate [120] or $[1\bar{2}0]$ orientation, both of which have c-axis out-of-plane growth. The above results thus show that we have multiple domains with either b- or c-axis out-of-plane growth within the same film.

© 2023 The Authors. Advanced Materials Interfaces published by Wiley-VCH GmbH

21967350, 2024, 3, Downloaded from https://onlinelibrary.wiley.com/doi/10.1002/admi.202300639 by Universidad De Zaragoza, Wiley Online Library on [12/02/2024]. See the Terms and Conditions (https://onlinelibrary.wiley.com/terms-and-conditions) on Wiley Online Library for rules of use; OA articles are governed by the applicable Creative Commons License

From the lamella prepared with $[2\bar{1}\bar{1}0]_{Al2O3}$ projection axis, only one monoclinic VO_2 domain orientation could be clearly identified as shown in Figure 4d,e, which has a hexagonal arrangement of O atoms around V. There are two possible zone-axes with such an arrangement of atoms, namely [010] with c-growth axis and [102] with b-growth axis. However, with the [010] zone-axis, the V atomic columns would form dimerized planes, i.e., with alternating short and long interplanar distances, which is not seen in this image. So the orientation must be [102] for which the simulations are shown to be in close agreement in Figure 4f,g. Apart from these domains which could be confirmed by comparing the V–V or V–O distances in the simulations, there were other domains, whose images are shown in Figure S7 (Supporting Information), which are significantly harder to verify since the V and O atomic columns are very close to each other such that they do not provide distinctly resolved signals in iDPC images.

An important observation from the images is that the domains are very small (often smaller than 5–10 nm) with no sharp boundaries, which means that many domains overlap in the image along the projection direction of the STEM imaging. The lamella have thicknesses of say 60 nm and then we would readily have six or more overlapping domains in TEM images, which would make it impossible to image any domain individually. In STEM, since the focusing is more confined at a certain depth (due to the "waist" of the focused electron beam) particularly since we can employ a large convergence angle in aberration-corrected STEM, it is still possible to distinguish some domains individually like we demonstrated above. Still, even in this case the very small domain size often leads to overlapping domains, making further analysis of these films very complex. Nevertheless, the presence of such small domains combined with the two possible out-of-plane axes seem to be a logical explanation why the MI transition is spread over a large temperature interval as shown in Figure 2e.[57]

2.3. VO_2 on $TiO_2(101)$

Cross-section lamella for samples on $TiO_2(101)$ were made with the long side of the lamella parallel to the (010) edge plane for STEM analysis of the sample which means perpendicular to the domain boundaries (such that the boundaries can be observed edge-on in the cross-section). In **Figure 5**a, we show the STEM HAADF image for the case where the VO_2 film was grown on TiO_2 at 500 °C. The contrast difference observed in the HAADF image shows three regions. A very thin (≈2 nm) top layer is very distinct, because it is clearly brighter than the regions below. Still, there is a ≈14 nm middle layer that is marginally brighter than the TiO_2 substrate at the bottom, which is observed along the [010] zone-axis as confirmed by the FFT in Figure 5c. In order to understand the origin of the three regions better, we performed EDS mapping of a selected area to capture these regions as shown in Figure 5d,e, with the elemental profiles of the line scan in Figure 5f. Note that the absolute values for atomic fractions in Figure 5f are generally not accurate, mainly due to spurious X-rays, but that the linescans still provide reliable qualitative information. In particular the three different regions can now be observed more distinctly, i.e., a pure VO_2 top layer of ≈2 nm thick, followed by a ≈14 nm thick middle layer where V has been diffused into the TiO_2 and finally the (pure) TiO_2 substrate at the bottom. The O percentage stays constant over the entire line scan which indicates that the three layers all have composition MO_2, where M is either V, Ti or some intermixed V_xTi_{1-x}. This intermixing layer also has the same (tetragonal) structure as TiO_2 as confirmed from the FFT in Figure 5b. Important to note that the intermediate layer does not show a typical diffusion profile where the V concentration is highest at the top and gradually reduces to zero inside the TiO_2 substrate. In contrast, the intermediate layer has relatively constant V to Ti concentration ratio (roughly being 0.1) and this $V_xTi_{1-x}O_2$ also shows a rather distinct interface with the pure TiO_2 substrate.

This sample with the ≈2 nm thick VO_2 top layer did not show any MIT due to the too limited layer thickness of VO_2. In order to reduce the thickness of the intermediate layer and to get thicker pure VO_2 films, the growth temperature was reduced in steps from 500 °C down to 350 °C. The HAADF images in Figure 5g–i confirm that this growth strategy works. Below a growth temperature of 400 °C, the intermediate layer is ≈3–4 nm thick and further reduction in growth temperature leads to an increase in VO_2 film thickness, but with no significant reduction in intermediate layer thickness. The films grown in the range 350–450 °C exhibited excellent MIT characteristics as shown in Figure S2 (Supporting Information) and discussed earlier. Overall, we see considerable V-Ti intermixing over the thickness range from ≈3 to ≈15 nm, which provides us with a new approach to make these superlattice structures by growing the VO_2 films at controlled temperatures in the range 350–450 °C. Further studies are required to study the properties of these heterostructures since the MIT characteristics should be affected by this intermediate intermixing layer.[45]

From a sample grown at 375 °C we produced multiple lamellas from areas with different domain widths. In **Figure 6**a, we show an overview drift-corrected frame integration (DCFI) image of a lamella taken with a camera length of 190 mm for better contrast. This allows us to clearly distinguish the (edge-on observed) domain boundaries, which are typically separated by a few 100 nm to ≈1 µm. A HAADF image of a domain boundary region is shown in Figure 6b. Focusing on the TiO_2 substrate, we see that its orientation is as expected [010] from the FFT in 6c. We see through FFTs in Figure 6d–f that the domain boundary region in fact contains two closely spaced parallel domain boundaries, i.e., that what looks at a distance like a single domain boundary is in fact a thin lamella of a domain, where its two boundaries make an angle of ≈50 degrees with the interface and surface. Note that this orientation is always inclined to one side and that the lamellae do not run at plus and minus 50 degrees through the film. This asymmetry agrees with the asymmetry induced by the substrate $TiO_2(101)$ where in this case the c-axis is oriented with a component to the left and the a-axis with a component to the right (see the indicated c- and a-axis in Figure 6b). Now the FFT analysis shows that the thin VO_2 lamella is viewed along the – $[010]_{M1}$ zone axis (FFT #3 in Figure 6) and that on both sides of the thin lamella the orientation of the two domains are actually identically corresponding to the $[102]_{M1}$ zone axis (FFT #2 and #4 in Figure 6). These structural differences are also observable more clearly in the DCFI-HAADF image shown in Figure S8a (Supporting Information). Note that even a more intricate

© 2023 The Authors. Advanced Materials Interfaces published by Wiley-VCH GmbH

21967350, 2024, 3, Downloaded from https://onlinelibrary.wiley.com/doi/10.1002/admi.202300639 by Universidad De Zaragoza, Wiley Online Library on [12/02/2024]. See the Terms and Conditions (https://onlinelibrary.wiley.com/terms-and-conditions) on Wiley Online Library for rules of use; OA articles are governed by the applicable Creative Commons License

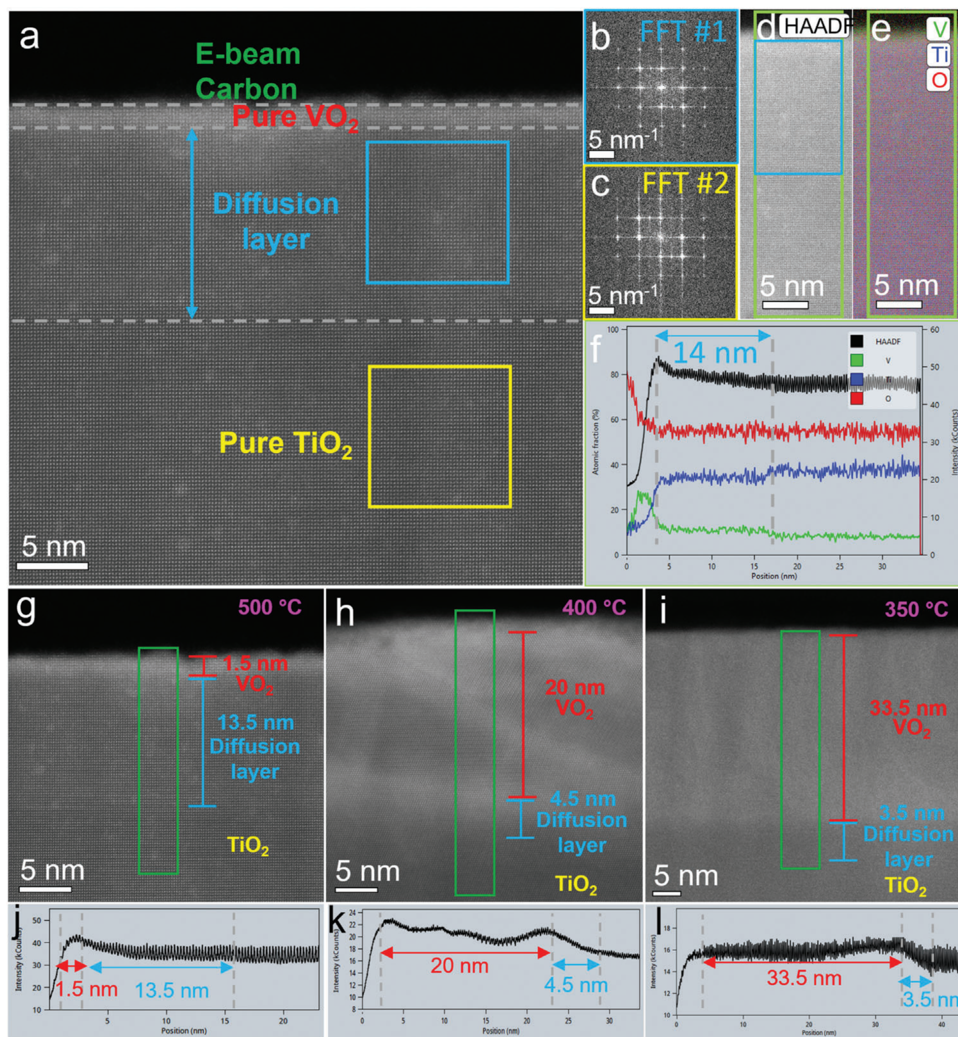

Figure 5. STEM HAADF images of VO_2 on TiO_2(101) grown at varying substrate temperatures from 500 to 350 °C, taken at 300 kV. a) VO_2 on TiO_2(101) grown at 500 °C viewed along [$\bar{1}$01] direction, and b,c) FFT of the intermixing region and pure TiO_2 region. The regions are confirmed using an EDS scan with the e) elemental mapping of a d) selected area, with f) its profile showing the variation of the different elements along the line scan. g–i) HAADF images of samples grown at 500, 400, and 350 °C, and j–l) respective profiles of the line scans.

structure is possible where the domain in the thin lamella is twinned with a boundary that runs perpendicular to the interface and surface of the film. So, in this case next to the $[010]_{M1}$ domain, also the $[0\bar{1}0]_{M1}$ domain is present, which has opposite orientation of the dimerized V–V planes in the monoclinic VO_2 structure. One such domain boundary region with both $[010]_{M1}$ and $[0\bar{1}0]_{M1}$ grains inside the thin lamella is also shown in Figure S8b (Supporting Information). These degenerate structures are equivalent to the non-degenerate original $[100]_R$ and $[\bar{1}00]_R$ orientations, which would obviously still be fully epitaxial with the tetragonal substrate. Hence, these domain boundaries are formed when the sample is being cooled down after growth, because the VO_2 grows fully epitaxially on the TiO_2 at the growth temperature where the VO_2 still has the same tetragonal structure as the TiO_2 substrate. However, when the VO_2 transforms during cooling from tetragonal to monoclinic the symmetry breaking causes the domain formation. Another important observation is that, although from the top-view of the sample the domain boundaries run perpendicular to the TiO_2(010) edge plane and seem parallel to the TiO_2(101) edge plane, the boundary plane is running inclined through the thickness of the film. This also explains the extended width of the domain boundaries when observed in the plan-view SEM image in Figure 2b.

In **Figure 7**a,b, we also show high-resolution HAADF and iDPC images of the sample taken at some distance away from domain boundaries, from which regions of VO_2 and TiO_2 have been cropped in Figure 7c,d,e,f, respectively. From the HAADF image, we can see that the film has excellent orientation matching with the substrate, and that the domains are essentially single-crystals. From the iDPC images, we see a hexagonal-like arrangement of O atoms around the central V or Ti atoms with the two V—O bonds perpendicular to c-axis being equal, but differ from the other four V—O bonds which are equal to each other. The observed atomic structures are in excellent agreement with the simulations done for the monoclinic (M1) $[102]_{VO2}$ and the tetragonal $[010]_{TiO2}$ orientations shown in Figure 7g–j. In summary, when we view for

© 2023 The Authors. Advanced Materials Interfaces published by Wiley-VCH GmbH

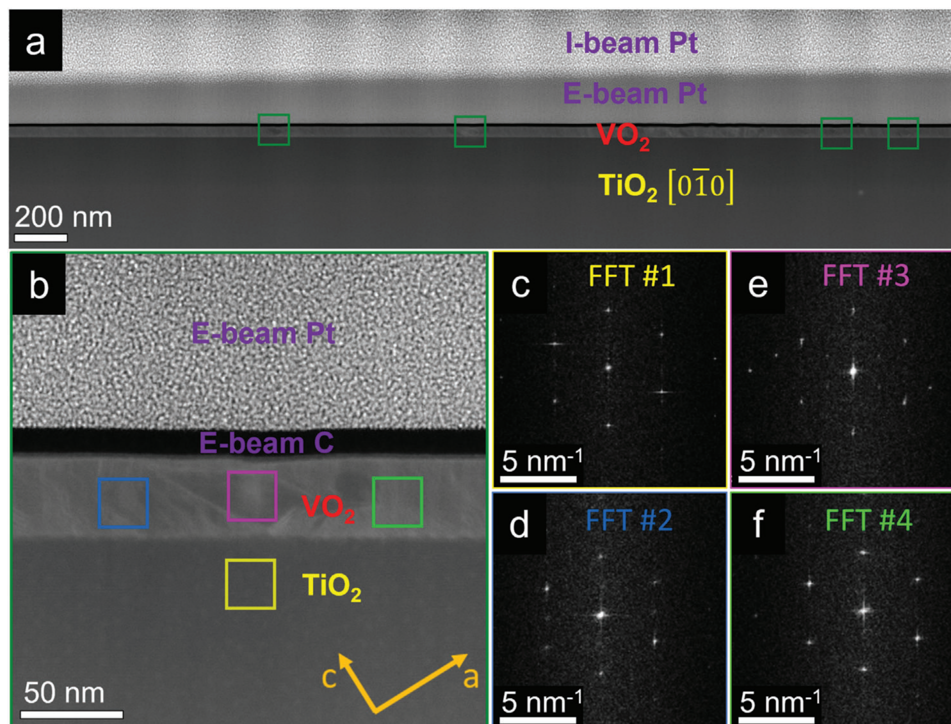

Figure 6. STEM-HAADF images of VO_2 on TiO_2 (101) substrate grown at 375 °C, taken at 300 kV. a) Overview HAADF-DCFI image showing the domain boundaries, one of which is shown in (b). The structures inside and outside the domain boundary are marked in, with FFTs 2–4 shown in (d–f), compared to the TiO_2 substrate with its FFT shown in (c).

the TiO_2(101) substrate along TiO_2[010], [102] domains are dominantly present and in between them a thin inclined domain of [010] and/or [0$\bar{1}$0] type is present.

2.4. VO_2 on TiO_2(001)

From Figure 2, we know that on TiO_2(001), the domain boundaries are parallel to the two orthogonal {110} edge planes of the substrate. Cross-section lamella were made from VO_2 grown at 375 °C, both parallel to one of the two edge planes and at the intermediate angle of 45° (rotation around out-of-plane TiO_2 c axis). In **Figure** 8a, we show an overview image of the lamella made parallel to the edge plane, so the zone-axis is [110]. We see multiple dark line running across the VO_2 film perpendicular to the VO_2/TiO_2 interface. These dark lines are ≈0.5-1 µm apart from each other which coincide well with the domain sizes observed in the SEM image in Figure 2c. However, when zooming in on the dark line in Figure 8b, it becomes obvious that the lines are not domain boundaries, but rather cracks developed in the film, which even can propagate considerably into the substrate (see Figure S9, Supporting Information). The FFT inset in the figure shows that the two sides of the boundary still have VO_2(1$\bar{1}$0) planes parallel to the crack boundary, but they have a small mutual rotation (around [110]) from each other due to the crack opening. These cracks have been reported to be thermally induced – when the sample cools down through the transition temperature, the cracks develop as a means of strain relaxation.[43,44,58]

We also show the overview of the cross-section made at 45° to the previous lamella in Figure 8c, where we see the cracks at a skew angle as our viewing axis is now [100]/]010] with the c-axis being the vertical direction in the images. Observing the structures around the cracks, we notice different sets of orientations from the inset FFTs of Figure 8d,e. Our films are predominantly composed of the M1 phase, but that in a follow-up paper, we can prove that there is a thin (≈2–3 nm thick region) close to the interface that contains the M2 phase. This region can be seen near the interface in **Figure 9**e between the clearly VO_2 M1 structure with dimerized V atoms, and the TiO_2 substrate. In Figure 9a,b,e,f, we show the HAADF and iDPC images of the two domains from Figure 8d, from which the domains have been cropped in Figure 9c (Crop#1 with the inset showing the HAADF image and the main image being the iDPC image) and 9 g (Crop#2 again with the inset showing the HAADF image and the main image being the iDPC image). In the first of these domains, we clearly see V atoms are aligned along c-axis marked with a red dashed line. These V atoms are also slightly elongated along c-axis as compared to the Ti atoms of the substrate. Also, as discussed previously, the V—O bonds perpendicular to the c-axis are equal, and they differ from the other four V—O bonds, which are also equal. This matches excellently to the $[102]_{M1}$ schematic model as shown in Figure 9i and the simulations of the iDPC with inset HAADF are shown in Figure 9d. On the other hand, in the second domain, we do not see the V atoms aligned along c-axis of the substrate as the Ti atoms are. Instead they align along the c-axis of the film marked with yellow dashed lines and therefore, have a structure with dimerized V–V planes.

 © 2023 The Authors. Advanced Materials Interfaces published by Wiley-VCH GmbH

21967350, 2024, 3, Downloaded from https://onlinelibrary.wiley.com/doi/10.1002/admi.202300639 by Universidad De Zaragoza, Wiley Online Library on [12/02/2024]. See the Terms and Conditions (https://onlinelibrary.wiley.com/terms-and-conditions) on Wiley Online Library for rules of use; OA articles are governed by the applicable Creative Commons License

ADVANCED MATERIALS INTERFACES
Open Access
www.advmatinterfaces.de

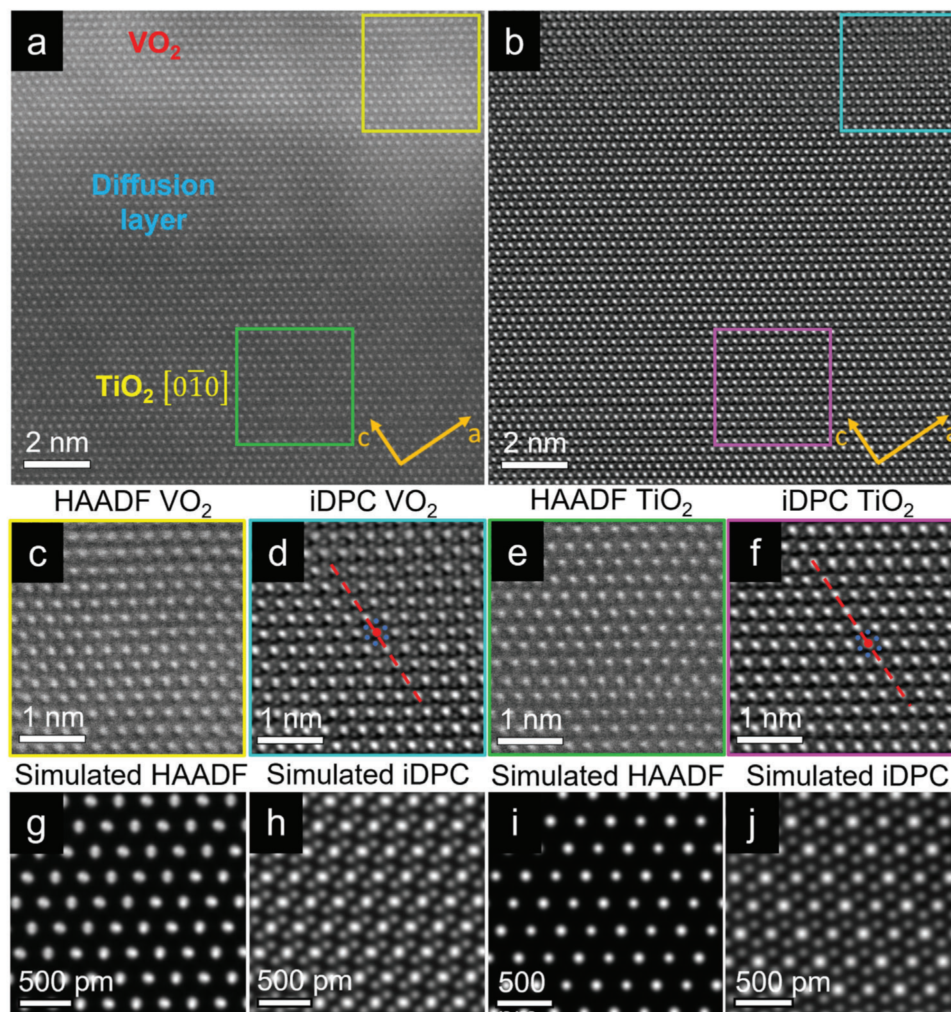

Figure 7. STEM HAADF and iDPC images of VO_2 on TiO_2(101) substrate grown at 375 °C, taken at 300 kV. a,b) HAADF and iDPC of the lamella away from domain boundaries, with cropped regions c,d) VO_2 and e,f) TiO_2 substrate for clarity showing epitaxial film (Red lines are to mark the c-axis in the image). Simulations of HAADF and iDPC for g,h) VO_2 with [102] orientation, and i,j) TiO2 with [010] orientation.

Consequently, all the 6 V—O bonds are now unequal which we find to match with the $[0\bar{1}0]_{M1}$ orientation which is confirmed by simulations shown in Figure 9h. The atomic structure observations for the first domain boundary (Figure 8d) are summarized in the schematic structure shown in Figure 9i. The results of a similar analysis of the second domain boundary shown in Figure 8e are summarized in the schematic shown in Figure 9j. Here it can be seen that both domains have the dimerized V–V planes, but there dimerization direction is mirrored(twinned) in the domain boundary. So, here we have the $[010]_{M1}$ and the $[0\bar{1}0]_{M1}$ orientations for both domains similar as observed for the thin domain boundary lamella observed in VO_2 on the TiO_2(101) substrate in Figure S8b (Supporting Information). Note that, unlike the [010] and $[0\bar{1}0]$ domains, the [102] and the $[\bar{1}0\bar{2}]$ domains are identical. So, three types of domains can be distinguished when we view along the TiO_2[100] (or equivalent TiO_2[010]).

So, when viewing along the $[110]_R$ zone-axis, we see a structure that is completely epitaxial and homogenous across the lamella, but, when viewing along $[100/010]_R$, we always see different orientations of VO_2 on the two sides of the cracks. These observations validate previous studies of the cracks developing as a stress relaxation mechanism[44,45] – all these grains have exactly the same rutile structure above the transition temperature, but as the thin film cools down, M1 VO_2 grains with different orientations nucleate and propagate until they meet resulting in stress which is only able to relax due to the formation of cracks. Overall, the presence of deep cracks in samples on (001) substrate results in relatively poor MIT characteristics, and thus VO_2 on this substrate is not suitable for electronic applications unless the stress can be tuned by external mechanisms like doping, or caused to relax with features other than cracks. Such an example does occur for the VO_2 film on the TiO_2(101) substrate, where despite very similar stress conditions due to similarly oriented domains, we observe intricate domain boundary structures instead of cracks. These domain boundary structures involve a thin lamella running inclined through the film at angle corresponding to a high resolved shear stress similar to stress relaxation in a slip system (or with deformation twinning), which enables

© 2023 The Authors. Advanced Materials Interfaces published by Wiley-VCH GmbH

21967350, 2024, 3, Downloaded from https://onlinelibrary.wiley.com/doi/10.1002/admi.202300639 by Universidad De Zaragoza, Wiley Online Library on [12/02/2024]. See the Terms and Conditions (https://onlinelibrary.wiley.com/terms-and-conditions) on Wiley Online Library for rules of use; OA articles are governed by the applicable Creative Commons License

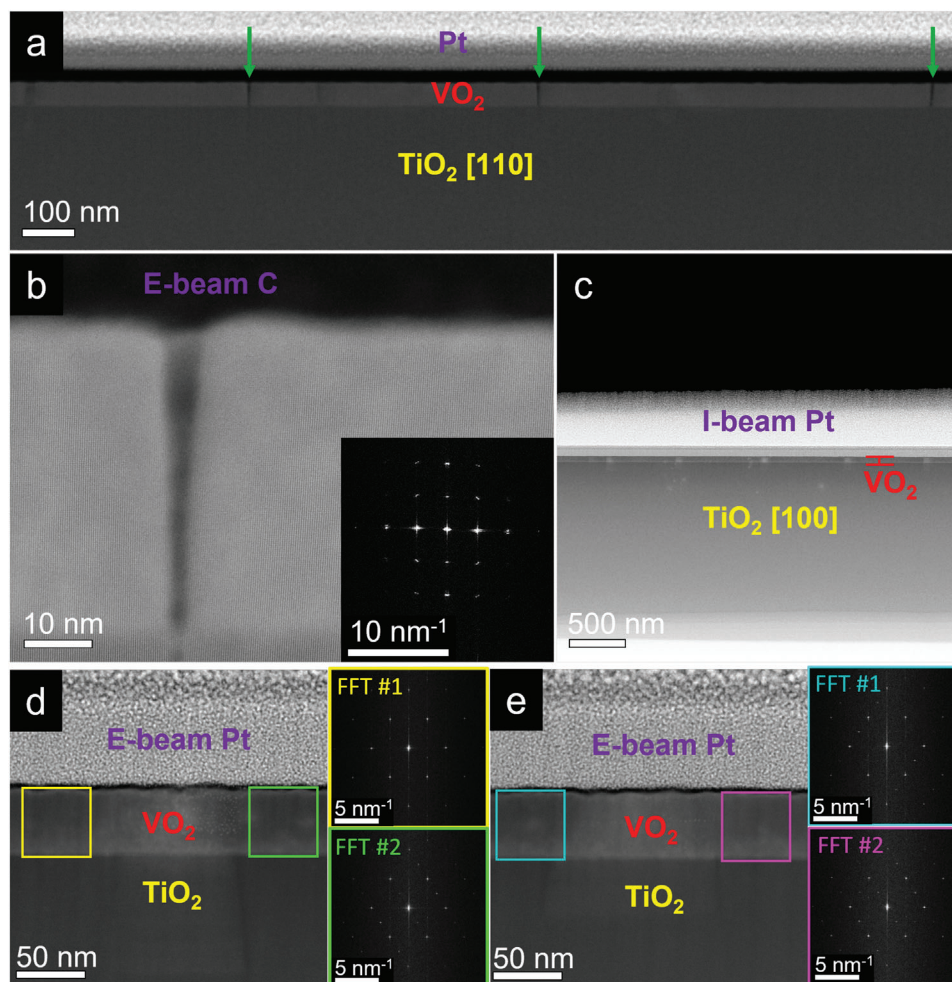

Figure 8. a) Overview (DCFI) HAADF image of cross-section of VO_2 on TiO_2 (001) grown at 375 °C along [110] projection which shows the features are actually cracks. b) HAADF of a crack with inset FFT. c) Overview of cross-section taken along [100]/[010] projection. d,e) HAADF of two of these domain boundaries where domains with different orientations (shown in the inset FFTs of the regions) meet.

plastic deformation.[59] When a boundary would run only perpendicular to the interface and surface, there is no resolved shear stress on the boundary plane and it cannot assist in any plastic deformation and the only response is cracking. Subsequently, without any cracks the MIT in VO_2 on TiO_2(101) remains of high quality, and this substrate should be highly suitable for electronic applications.

3. Conclusion

In summary, we have scrutinized the microstructure of VO_2 films grown on different substrates using in particular advanced STEM characterization, also allowing imaging of oxygen atomic columns, and have correlated these microstructures with the observed metal-insulator transition (MIT) properties as measured using van-der-Pauw sheet resistance measurements. Based on our analysis, we conclude that VO_2 films grown on c-sapphire consist of very small columnar domains (with column diameters of only 5–10 nm) leading to an MIT spread over a wide temperature range. The monoclinic (M1) VO_2 films grown on rutile TiO_2 contain micrometer sized domains having boundaries along (110) planes. Cracks between domains are observed on the (001) substrate, but not on the (101) substrate. It is expected that the VO_2 films grown with the rutile structure at elevated temperature are fully lattice matched with the rutile TiO_2 and that the cracks develop during cooling to room temperature when the rutile to M1 phase transition occurs in the VO_2 films. An intricate domain boundary structure is observed in the VO_2 on TiO_2(101) that seems to be responsible for the plastic deformation preventing cracking. As a result, we get limited electrical conductivity across the film and relatively poor MIT characteristics for VO_2 on TiO_2(001), but excellent MIT characteristics for VO_2 on TiO_2(101), which is therefore a promising platform for electrical devices.

At 500 °C hardly any VO_2 film grows on TiO_2, but instead a sizeable interdiffusion layer (≈15 nm thick) is formed, i.e., where V diffuses into rutile TiO_2. Below 400 °C, the intermediate layer is ≈3-4 nm thick and further reduction in growth temperature leads to an increase in VO_2 film thickness, but with no significant reduction in interdiffusion layer thickness. These results show that

© 2023 The Authors. Advanced Materials Interfaces published by Wiley-VCH GmbH

21967350, 2024, 3, Downloaded from https://onlinelibrary.wiley.com/doi/10.1002/admi.202300639 by Universidad De Zaragoza, Wiley Online Library on [12/02/2024]. See the Terms and Conditions (https://onlinelibrary.wiley.com/terms-and-conditions) on Wiley Online Library for rules of use; OA articles are governed by the applicable Creative Commons License

21967350, 2024, 3, Downloaded from https://onlinelibrary.wiley.com/doi/10.1002/admi.202300639 by Universidad De Zaragoza, Wiley Online Library on [12/02/2024]. See the Terms and Conditions (https://onlinelibrary.wiley.com/terms-and-conditions) on Wiley Online Library for rules of use; OA articles are governed by the applicable Creative Commons License

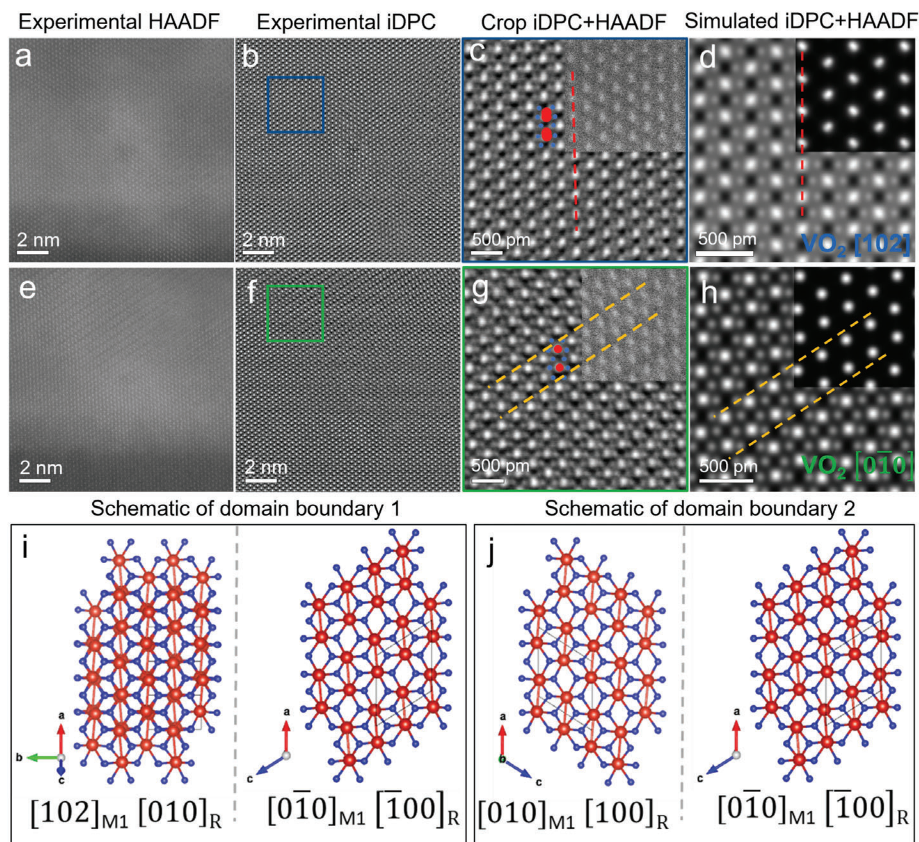

Figure 9. HAADF and iDPC of domains 1 and 2 from Figure 8d are shown in (a,b) and (e,f), with the relevant domains cropped and shown in (c,g) with their corresponding simulations in (d,h) respectively. This gives us the schematic of the domains across the cracks from Figure 8d,e shown in (i,j).

the MIT of the VO_2 top film contains an additional tunable parameter by varying the thickness and composition of the interdiffusion layer. As a next step our goal is to perform comprehensive STEM-iDPC(+HAADF) analysis to monitor the atomic structure changes of the VO_2 by in situ heating and cooling during the MIT.

4. Experimental Section

Pulsed Laser Deposition: Epitaxial VO_2 films were grown on single-crystal c-cut sapphire (0001), rutile TiO_2 (101), and (001) substrates using pulsed laser deposition (PLD). A KrF excimer laser ($\lambda = 248$ nm) was focused on a Vanadium metal target (99.9% pure) with a fluence of $\approx$2.5 J cm^{-2} and pulse rate of 10 Hz, in a vacuum chamber kept at a base pressure $<10^{-7}$ mbar throughout the deposition. Growth parameters like the number of pulses, substrate temperature, and oxygen pressure (P_{O2}) were varied, resulting in stoichiometric VO_2 films of varying thickness and quality.

Van der Pauw Sheet Resistance Measurements: The van der Pauw technique was used to measure the sheet resistance of the thin films. This method can be applied for any thin film of arbitrary shape which is of uniform thickness and has no holes, and the resistance so obtained is not affected by contact resistances.[60] Four probes of silver were placed at the perimeter (as close to the boundary as possible) and electrical measurements were done using a Keithley setup to obtain the horizontal ($R_{horizontal}$) and vertical resistances ($R_{vertical}$), from which the sheet resistance (R_s) was calculated.

X-Ray Diffraction: 2θ-ω scans were performed using a Panalytical X'pert Pro MRD X-ray diffractometer using a normal stage at room temperature over a wide range of 2θ from 20° to 100°, and then with a heater stage at 2θ values around major substrate peaks to determine the crystal structure of the film before transition (at room temperature), and after transition (at 150 °C). Reciprocal space maps (2θ-ω two-axis measurements) around the major peaks of the substrates were also recorded to find out the epitaxial relationship of the film in-plane on the substrate.

Specimen Preparation for Microscopy: A Helios G4 CX Dual-Beam system with a Ga-focused ion beam (FIB) was used to prepare cross-section lamella from the samples. A clean area (15 µm x 1.5 µm) was carefully chosen on the thin film surface from which the cross-section will be prepared. A protective coating must be deposited over the selected area to prevent ion radiation damage and sample damage or amorphization. Since ion-beam platinum deposition can also damage the very top surface of the sample ($\approx$50 nm, which already exceeds the sample thickness), electron-beam Carbon and electron-beam Platinum were deposited first at a very slow rate. Bulk ion milling was performed to reveal the shape of the lamella, and intermediate milling was done with a small tilt of ± 1.5° to thin the lamella to a thickness of $\approx$1–1.5 µm. A U-shaped cut was applied to make the lamella almost free except at one side, and then the lift-out procedure was performed using a manipulator. The lamella was welded to a TEM grid and was ready for subsequent thinning. Thinning was performed on a Peltier-cooled chip, initially with a high voltage of 30 kV up to a thickness of $\approx$100 nm. Low kV (5 and 2 kV) thinning was then done to remove the surface amorphization until lamella became electron transparent.

Scanning Transmission Electron Microscopy (STEM): The lamellas prepared were cleaned using plasma for 5–10 min before inserting in the

© 2023 The Authors. Advanced Materials Interfaces published by Wiley-VCH GmbH

microscope column of a probe- and image-corrected ThermoFisher Scientific ThemisZ S/TEM equipment operated at 300 kV, for STEM imaging and elemental mapping. The STEM alignments were done on the amorphous Platinum top layer. Aberrations were corrected up to the fourth order using the TEAM software, and fine-tuning of twofold condenser astigmatism was done using Sherpa software in order to achieve a resolution of ≈64 pm. Defocus values were generally set to negative values from 0 to -10 nm for imaging. For iDPC imaging,[48,61] the gain of the four segments was adjusted to equal intensity background levels to get no deflection of the beam through the amorphous Pt layer.

A semi-convergence angle of ≈21–25 mrad was used to get a small depth of focus. The pixel dwell-time was varied between 1 and 10 µs, with the image resolution as 1024×1024, 2048×2048, or 4096×4096 pixels. The images obtained were filtered using either Radial Wiener filter or Gaussian filter to get HAADF and iDPC images used for analysis.

Multi-Slice Simulations: Models of monoclinic and rutile phase of VO_2 with the parameters given in Tables S4 and S5 (Supporting Information), were made using VESTA and exported as cif files. These models were then used in the Dr. Probe software[62] for STEM HAADF and iDPC image simulations of the structures along different orientations. For the simulations, all aberrations except for defocus (kept at -4 nm) were neglected, and the other microscope parameters were set to experimental values (see Table S7, Supporting Information).

Supporting Information

Supporting Information is available from the Wiley Online Library or from the author.

Acknowledgements

The authors would like to acknowledge the support of Prof. Dr. Beatriz Noheda from the Zernike Institute for Advanced Materials, University of Groningen, and her group members Jacob Baas and Dr. Qikai Guo.

Conflict of Interest

The authors declare no conflict of interest.

Author Contributions

A.A. and B.J.K. conceived the idea. A.A. fabricated the thin films and performed all characterization measurements. Training for pulsed laser deposition and optimization of thin films was done with the help of H.Z. STEM measurements were done by P.K. on c-sapphire and by A.A. on the other substrates along with M.A. who was also critical for the analysis of STEM data. A.A. performed the simulations and wrote the paper, which was primarily edited by B.J.K. with critical inputs from the other authors.

Data Availability Statement

The data that support the findings of this study are available from the corresponding author upon reasonable request.

Keywords

metal–insulator transition, pulsed laser deposition, scanning transmission electron microscopy, VO_2 epitaxial thin films

Received: July 28, 2023
Revised: September 29, 2023
Published online: December 11, 2023

[1] N. F. Mott, *Rev. Mod. Phys.* **1968**, *40*, 677.
[2] M. Imada, A. Fujimori, Y. Tokura, *Rev. Mod. Phys.* **1998**, *70*, 1039.
[3] T. Driscoll, S. Palit, M. M. Qazilbash, M. Brehm, F. Keilmann, B. G. Chae, S. J. Yun, H. T. Kim, S. Y. Cho, N. M. Jokerst, D. R. Smith, D. N. Basov, *Appl. Phys. Lett.* **2008**, *93*, 024101.
[4] E. Strelcov, Y. Lilach, A. Kolmakov, *Nano Lett.* **2009**, *9*, 2322.
[5] M. Seo, J. Kyoung, H. Park, S. Koo, H. S. Kim, H. Bernien, B. J. Kim, J. H. Choe, Y. H. Ahn, H. T. Kim, N. Park, Q. H. Park, K. Ahn, D. S. Kim, *Nano Lett.* **2010**, *10*, 2064.
[6] B. Hu, Y. Ding, W. Chen, D. Kulkarni, Y. Shen, V. V. Tsukruk, Z. L. Wang, *Adv. Mater.* **2010**, *22*, 5134.
[7] F. J. Morin, *Phys. Rev. Lett.* **1959**, *3*, 34.
[8] J. B. Goodenough, *J. Solid State Chem.* **1971**, *3*, 490.
[9] J. Laverock, S. Kittiwatanakul, A. Zakharov, Y. Niu, B. Chen, S. A. Wolf, J. W. Lu, K. E. Smith, *Phys. Rev. Lett.* **2014**, *113*, 216402.
[10] S. Kumar, J. P. Strachan, M. D. Pickett, A. Bratkovsky, Y. Nishi, R. S. Williams, *Adv. Mater.* **2014**, *26*, 7505.
[11] G. Villeneuve, A. Bordet, A. Casalot, J. P. Pouget, H. Launois, P. Lederer, *J. Phys. Chem. Solids* **1972**, *33*, 1953.
[12] J. P. Pouget, H. Launois, T. M. Rice, P. Dernier, A. Gossard, G. Villeneuve, P. Hagenmuller, *Phys. Rev. B* **1974**, *10*, 1801.
[13] J. P. Pouget, H. Launois, J. P. D'Haenens, P. Merenda, T. M. Rice, *Phys. Rev. Lett.* **1975**, *35*, 873.
[14] D. Lee, B. Chung, Y. Shi, G.-Y. Kim, N. Campbell, F. Xue, K. Song, S.-Y. Choi, J. P. Podkaminer, T. H. Kim, P. J. Ryan, J.-W. Kim, T. R. Paudel, J.-H. Kang, J. W. Spinuzzi, D. A. Tenne, E. Y. Tsymbal, M. S. Rzchowski, L. Q. Chen, J. Lee, C. B. Eom, *Science* **2018**, *362*, 1037.
[15] R. M. Wentzcovitch, W. W. Schulz, P. B. Allen, *Phys. Rev. Lett.* **1994**, *72*, 3389.
[16] M. Gatti, F. Bruneval, V. Olevano, L. Reining, *Phys. Rev. Lett.* **2007**, *99*, 266402.
[17] J. Laverock, A. R. H. Preston, D. Newby, K. E. Smith, S. Sallis, L. F. J. Piper, S. Kittiwatanakul, J. W. Lu, S. A. Wolf, M. Leandersson, T. Balasubramanian, *Phys. Rev. B* **2012**, *86*, 195124.
[18] M. W. Haverkort, Z. Hu, A. Tanaka, W. Reichelt, S. V. Streltsov, M. A. Korotin, V. I. Anisimov, H. H. Hsieh, H.-J. Lin, C. T. Chen, D. I. Khomskii, L. H. Tjeng, *Phys. Rev. Lett.* **2005**, *95*, 196404.
[19] T. Driscoll, H. T. Kim, B. G. Chae, M. di Ventra, D. N. Basov, *Appl. Phys. Lett.* **2009**, *95*, 043503.
[20] T. Driscoll, H.-T. Kim, B.-G. Chae, B.-J. Kim, Y.-W. Lee, N. M. Jokerst, S. Palit, D. R. Smith, M. di Ventra, D. N. Basov, *Science* **2009**, *325*, 1518.
[21] A. Cavalleri, C. Tóth, C. W. Siders, J. A. Squier, F. Ráksi, P. Forget, J. C. Kieffer, *Phys. Rev. Lett.* **2001**, *87*, 237401.
[22] J. Jeong, N. Aetukuri, T. Graf, T. D. Schladt, M. G. Samant, S. S. P. Parkin, *Science* **2013**, *339*, 1402.
[23] K. Lai, M. Nakamura, W. Kundhikanjana, M. Kawasaki, Y. Tokura, M. A. Kelly, Z.-X. Shen, *Science* **2010**, *329*, 190.
[24] A. Romanyuk, R. Steiner, L. Marot, P. Oelhafen, *Sol. Energy Mater. Sol. Cells* **2007**, *91*, 1831.
[25] J. Wei, H. Ji, W. Guo, A. H. Nevidomskyy, D. Natelson, *Nat. Nanotechnol.* **2012**, *7*, 357.
[26] W. P. Hsieh, M. Trigo, D. A. Reis, G. Andrea Artioli, L. Malavasi, W. L. Mao, *Appl. Phys. Lett.* **2014**, *104*, 021917.
[27] C. Marini, L. Baldassarre, M. Baldini, A. Perucchi, D. di Castro, L. Malavasi, S. Lupi, P. Postorino, *High Press. Res.* **2010**, *30*, 55.
[28] D. H. Kim, H. S. Kwok, *Appl. Phys. Lett.* **1994**, *65*, 3188.
[29] D.-H. Youn, H.-T. Kim, B.-G. Chae, Y.-J. Hwang, J.-W. Lee, S.-L. Maeng, K.-Y. Kang, *J. Vac. Sci. Technol., A* **2004**, *22*, 719.
[30] S. Yu, S. Wang, M. Lu, L. Zuo, *J. Appl. Phys.* **2017**, *122*, 235102.
[31] M. K. Behera, D. K. Pradhan, S. K. Pradhan, A. K. Pradhan, *J. Appl. Phys.* **2017**, *122*, 245110.
[32] B. Hong, Y. Yang, K. Hu, Y. Dong, J. Zhou, Y. Zhang, W. Zhao, Z. Luo, C. Gao, *Appl. Phys. Lett.* **2019**, *115*, 251605.

© 2023 The Authors. Advanced Materials Interfaces published by Wiley-VCH GmbH

21967350, 2024, 3, Downloaded from https://onlinelibrary.wiley.com/doi/10.1002/admi.202300639 by Universidad De Zaragoza, Wiley Online Library on [12/02/2024]. See the Terms and Conditions (https://onlinelibrary.wiley.com/terms-and-conditions) on Wiley Online Library for rules of use; OA articles are governed by the applicable Creative Commons License

[33] C. V. Thompson, R. Carel, *J Mech Phys Solids* **1996**, *44*, 657.
[34] J. Y. Suh, R. Lopez, L. C. Feldman, R. F. Haglund, *J. Appl. Phys.* **2004**, *96*, 1209.
[35] J. Cao, Y. Gu, W. Fan, L. Q. Chen, D. F. Ogletree, K. Chen, N. Tamura, M. Kunz, C. Barrett, J. Seidel, J. Wu, *Nano Lett.* **2010**, *10*, 2667.
[36] P. Jin, K. Yoshimura, S. Tanemura, *J. Vac. Sci. Technol., A* **1997**, *15*, 1113.
[37] D. Brassard, S. Fourmaux, M. Jean-Jacques, J. C. Kieffer, M. A. el Khakani, *Appl. Phys. Lett.* **2005**, *87*, 051910.
[38] F. Guinneton, L. Sauques, J. C. Valmalette, F. Cros, J. R. Gavarri, *J. Phys. Chem. Solids* **2005**, *66*, 63.
[39] G. Xu, P. Jin, M. Tazawa, K. Yoshimura, *Appl. Surf. Sci.* **2005**, *244*, 449.
[40] J. Narayan, V. M. Bhosle, *J. Appl. Phys.* **2006**, *100*, 103524.
[41] J. Lappalainen, S. Heinilehto, S. Saukko, V. Lantto, H. Jantunen, *Sens Actuators A Phys* **2008**, *142*, 250.
[42] J. Jian, A. Chen, Y. Chen, X. Zhang, H. Wang, *Appl. Phys. Lett.* **2017**, *111*, 153102.
[43] K. Nagashima, T. Yanagida, H. Tanaka, T. Kawai, *Phys Rev B Condens Matter Mater Phys* **2006**, *74*, 172106.
[44] J. O. Krisponeit, S. Fischer, S. Esser, V. Moshnyaga, T. Schmidt, L. F. J. Piper, J. I. Flege, J. Falta, *Sci. Rep.* **2020**, *10*, 22374.
[45] L. Chen, Y. Cui, H. Luo, Y. Gao, *J. Phys. Chem. C* **2022**, *126*, 6016.
[46] Y. Cho, S. Aritomi, T. Kanki, K. Kinoshita, N. Endo, Y. Kondo, D. Shindo, H. Tanaka, Y. Murakami, *Mater. Res. Bull.* **2018**, *102*, 289.
[47] Y. Muraoka, Z. Hiroi, *Appl. Phys. Lett.* **2002**, *80*, 583.
[48] I. Lazić, E. G. T. Bosch, S. Lazar, *Ultramicroscopy* **2016**, *160*, 265.
[49] Z. P. Wu, S. Yamamoto, A. Miyashita, Z. J. Zhang, K. Narumi, H. Naramoto, *J. Phys.: Condens. Matter* **1998**, *10*, L765.
[50] Y. Shigesato, M. Enomoto, H. Odaka, *Jpn. J. Appl. Phys.* **2000**, *39*, 6016.
[51] T. H. Yang, R. Aggarwal, A. Gupta, H. Zhou, R. J. Narayan, J. Narayan, *J. Appl. Phys.* **2010**, *107*, 053514.
[52] Y. Cui, S. Ramanathan, *J. Vac. Sci. Technol., A* **2011**, *29*, 041502.
[53] F. Sandiumenge, L. Rodríguez, M. Pruneda, C. Magén, J. Santiso, G. Catalan, *Adv. Mater.* **2021**, *33*, 2004374.
[54] Y. Sharma, M. V. Holt, N. Laanait, X. Gao, I. N. Ivanov, L. Collins, C. Sohn, Z. Liao, E. Skoropata, S. V. Kalinin, N. Balke, G. Eres, T. Z. Ward, H. N. Lee, *APL Mater.* **2019**, *7*, 081127.
[55] Y. Zhao, J. Hwan Lee, Y. Zhu, M. Nazari, C. Chen, H. Wang, A. Bernussi, M. Holtz, Z. Fan, *J. Appl. Phys.* **2012**, *111*, 053533.
[56] L. L. Fan, Y. F. Wu, C. Si, G. Q. Pan, C. W. Zou, Z. Y. Wu, *Appl. Phys. Lett.* **2013**, *102*, 011604.
[57] X. Li, A. Gloter, H. Gu, X. Cao, P. Jin, C. Colliex, *Acta Mater.* **2013**, *61*, 6443.
[58] X. Chen, S. Kittiwatanakul, Y. Cheng, T. V. Slusar, A. S. Mcleod, Z. Li, H.-T. Kim, D. N. Basov, M. Liu, *Appl. Phys. Lett.* **2022**, *121*, 021902.
[59] J. M. Rosenberg, H. R. Piehler, *Metall. Trans.* **1971**, *2*, 257.
[60] L. J. van der Pauw, *Philips Tech. Rev.* **1958**, *20*, 220.
[61] N. H. Dekkers, H. de Lang, *Optik* **1974**, *41*, 452.
[62] J. Barthel, *Ultramicroscopy* **2018**, *193*, 1.

© 2023 The Authors. Advanced Materials Interfaces published by Wiley-VCH GmbH

21967350, 2024, 3, Downloaded from https://onlinelibrary.wiley.com/doi/10.1002/admi.202300639 by Universidad De Zaragoza, Wiley Online Library on [12/02/2024]. See the Terms and Conditions (https://onlinelibrary.wiley.com/terms-and-conditions) on Wiley Online Library for rules of use; OA articles are governed by the applicable Creative Commons License